

Functional Organization of Temporal Frequency Selectivity in Primate Visual Cortex

Ilya Khaytin^{1,2}, Xin Chen³, David W. Royal³, Octavio Ruiz³, Walter J. Jermakowicz^{1,2}, Ralph M. Siegel⁴ and Vivien A. Casagrande^{3,5,6}

¹Medical Sciences Training Program, ²Cognitive and Integrative Neuroscience Program, and, ³Department of Cell and Developmental Biology, Vanderbilt University, Nashville, TN 37232, ⁴Center for Molecular and Behavioral Neuroscience, Rutgers University, Newark, NJ 07102, ⁵Departments of Psychology and ⁶Ophthalmology and Visual Science, Vanderbilt University, Nashville, TN 37232

Several studies have shown that neurons with similar response properties are arranged together in domains across primary visual cortex (V1). An orderly pattern of domains has been described for preferences to ocular dominance, orientation, and spatial frequency. Temporal frequency preference, another important attribute of the visual scene, also might be expected to map into different domains. Using optical imaging and a variety of quantitative methods, we examined how temporal frequency selectivity is mapped in V1 of the prosimian primate, bush baby (*Otolemur garnetti*). We found that unlike other attribute maps, selectivity for different temporal frequencies is arranged *uniformly* across V1 with no evidence of local clustering. Global tuning for temporal frequency, based on magnitude of response, showed a good match to previous tuning curves for single neurons. A peak response was found around 2.0 Hz, with smaller attenuation at lower temporal frequencies than at higher frequencies. We also examined whether the peak temporal frequency response differed between anatomical compartments defined by cytochrome oxidase (CO). No significant differences in the preference for temporal frequency were found between these CO compartments. Our findings show that key sensory attributes that are linked in perception can be organized in quite distinct ways in V1 of primates.

Keywords: bush baby, columns, cytochrome oxidase, optical imaging, orientation preference, striate cortex

Introduction

Based on their pioneering investigations of neuronal response properties in primary visual cortex (V1), Hubel and Wiesel (1974a) proposed the well-known “ice cube” model to explain how fundamental visual features are represented in the brain. This model posits that a small patch of the cortex is devoted to systematically representing all relevant sensory information from a small region of the sensory environment and that adjacent patches of the cortex represent adjacent regions of visual space. According to their model, which has largely been confirmed for primates using both single-unit recording and optical imaging (Hubel and Wiesel 1962, 1968, 1974b; Bonhoeffer and Grinvald 1991; LeVay and Nelson 1991; Blasdel 1992; Bonhoeffer et al. 1995; Hubener et al. 1997; Shoham et al. 1997; Issa et al. 2000; Xu, Bosking, et al. 2004; Xu et al. 2005), different sensory attributes such as ocular dominance, orientation selectivity, and spatial frequency selectivity are represented systematically in domains or columns in which neurons that are tuned to similar preferences, representing the same part of visual space, lie adjacent.

As more and more columnar systems have been discovered, it has become increasingly important to establish if there are

common rules that govern the geometric relationships between different column systems, particularly those which are key to the representation of features of the visual scene such as orientation and spatial and temporal frequencies. For example, in all primates examined including the bush baby (the subject of the current study), different orientation preferences are grouped into “domains,” that is, patches of the cortex that run along smoothly varying contours. Some of these feature domains are locally orthogonal to each other, and a discontinuity in one domain occurs in the smoothest part of the others (Weliky et al. 1996; Hubener et al. 1997; Everson et al. 1998; Xu et al. 2005, 2007). A similar pattern is seen in most other species with the exception of rodents where orientation preferences curiously show no domain structure, suggesting that a different set of rules apply (Van Hooser et al. 2005, 2006). For spatial frequency selectivity, domain-like structures also have been identified in the bush baby and in the cat, but whether this is the rule has been the subject of some controversy (Berardi et al. 1982; Bonhoeffer et al. 1995; Shoham et al. 1997; Everson et al. 1998; Issa et al. 2000).

Thus far, the only optical imaging study that measured temporal frequency selectivity was done in the cat visual cortex, and that study did not systematically study the distribution of temporal frequency preferences (Shoham et al. 1997). Using single-unit recording, DeAngelis et al. (1999) found some evidence to suggest that there may be clustering of neurons with similar temporal frequency preference. Surprisingly, however, no data are available in any species that have directly addressed the issue of how temporal frequency selectivity is mapped across visual cortex, and if temporal frequency selectivity is organized into domains, how such domains are organized. Given the importance of both spatial and temporal frequencies as attributes defining the visual scene, it is critical to know whether common rules govern their organization, and if not, how temporal frequency tuning is mapped in relationship to other sensory properties. Specifically, in this study, we quantitatively examined whether temporal frequency tuning, like spatial frequency tuning, ocular dominance, and orientation preference (Xu et al. 2003, 2005, 2007), is organized into domains in the prosimian bush baby. If so, how do the maps of temporal frequency selectivity relate to other anatomical markers or modules proposed to represent different functions, such as cytochrome oxidase (CO) blobs?

We had 3 predictions which are outlined in Figure 1. First, if temporal frequency preference is inseparable from orientation preference, then both the location and size of orientation preference domains should change depending on the fundamental temporal frequency of the stimulus (Fig. 1A). Second, if

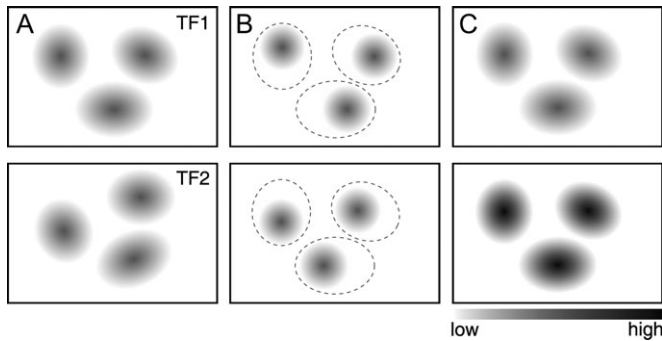


Figure 1. Three predictions concerning the relationship between temporal frequency and orientation preference domains. Orientation domains are shown as gray toned areas with increasing signal strength indicated by darker gray tones. TF1 and TF2 refer to 2 different temporal frequencies. (A) If orientation tuning depends on temporal frequency tuning, the prediction is that orientation domains shift with different temporal frequencies as shown by the changes in domain positions from the top to the bottom panel. (B) If orientation tuning does not depend on temporal frequency tuning, but groups of cells with different temporal frequency preferences cluster together, the prediction is that orientation domains would remain in the same positions (dashed lines) but that the area of strongest response within each domain would shift with change in temporal frequency of the stimuli. Again compare the top with the bottom panel. (C) If orientation tuning of the cells does not depend on temporal frequency tuning and cells with different temporal frequency preferences are distributed uniformly across cortex, the prediction is that the only change would be a change in the strength of response with changing temporal frequency of the stimuli. In this example, the 3 orientation domains shown are more responsive in the bottom panel (one temporal frequency) than in the top panel (another temporal frequency).

temporal frequency preference is independent of orientation but the former is arranged into domains, we should see shifts in the location of maximal response within the same orientation domain at different temporal frequencies (Fig. 1B). Finally, if temporal frequency preference is uniformly distributed across V1, we should see no change in orientation domain locations or in their sizes. In the latter case, the most significant difference in response would be a change in response magnitude with different temporal frequencies (Fig. 1C, see also DeBruyn et al. 1993).

Methods

Animals

Seven bush babies (*Otolemur garnetti*) of both sexes, which were raised in our colony, were used in these experiments. They were housed and handled according to approved protocols from the Institutional Animal Care and Use Committee at Vanderbilt University. Of these animals, 4 were used in acute experiments and 3 had initial surgery and then retinotopic optical mapping and temporal frequency mapping done in separate survival sessions before the final acute experiment during which the bulk of data were collected. A total of 7 hemispheres were imaged.

Surgery and Perfusion

All experiments were conducted under general anesthesia and paralysis. In acute experiments, anesthesia was induced with 2–4% isoflurane in O₂. At the same time, animals were given intramuscular injections of dexamethasone (1 mg/kg), glycopyrrolate (Robinul 0.015 mg/kg), and ceftiofur sodium (Naxcel 2.2 mg/kg), and 2 venous catheters were inserted. Animals were intubated and mounted in a stereotaxic apparatus. Prior to induction of neuromuscular blockade (NMB), animals were connected to temperature, electrocardiography, and expired CO₂ probes, and baseline readings were taken. All optical imaging experiments were conducted under propofol/nitrous oxide anesthesia and NMB. Once all preparatory steps were undertaken,

animals were switched from isoflurane to propofol and allowed at least 15 min to remain in a stable plane of anesthesia before NMB, which was induced with an injection of 0.7–1.0 mg/kg of vecuronium bromide. Animals were respired with a ventilator delivering a 3:1 mixture of NO₂ and O₂ at a sufficient rate to maintain expired CO₂ at 4%.

During the surgery, anesthesia was maintained using propofol, delivered at approximately 10 mg/kg/h. During the experiment, the amount of propofol delivered was reduced to 4–7 mg/kg/h. NMB was maintained with vecuronium bromide (0.6 mg/kg/h) in a 5.0% dextrose lactated Ringers solution. An opening approximately 10 mm in diameter was made over V1 centered at 8 mm from the posterior pole and 9 mm from the midline. The dura was removed and replaced with an artificial dura (Tecoflex), as described by Sakas et al. (1990). The opening was covered with 1% agarose in saline and sealed with a glass coverslip. In chronic experiments, all procedures were carried out under sterile conditions. The first session in these experiments was reserved for the craniotomy of the area above V1 and Tecoflex placement and was conducted under isoflurane in O₂ anesthesia (1–3%) without paralysis. No imaging data were collected during this first surgical session. In the chronic experiments, at the end of each imaging session, animals were weaned from the ventilator after infusion of paralytic was stopped and were watched carefully until they were capable of eating and drinking on their own. These animals also were given the analgesic, buprenorphine (Buprenex 0.01 mg/kg), and the antibiotic, ceftiofur sodium (2.2 mg/kg), postoperatively.

Pupils were dilated with 2% cyclopentolate (Cyclogyl) and/or 1% atropine drops, and contact lenses with sufficient power and 3-mm pupils were used to make the retina conjugate with the viewing distance to the monitor of 28.5 cm. Retinal landmarks including the optic disks and *area centralii* were plotted using back reflection from the tapetum prior to the start of each experiment.

Histology and Alignment

Before each imaging session, a series of color images of the brain were taken using a handheld digital camera. These images, along with reference images taken with the optical imaging camera, later were used to aid in aligning the histological sections with the optical images. At the termination of each experiment, the animal was euthanized with an overdose of sodium pentobarbital (Nembutal, 50 mg/kg) and perfused through the heart, first with a saline rinse containing 0.05% sodium nitrite and then with a fixative solution containing 2% paraformaldehyde in 0.1 M phosphate buffer. The brain was removed and flattened using the following procedure. First, the occipital cortex was cut from the rest of the brain in a coronal plane. Next, the medial wall (invisible to the camera) was trimmed so that the cut was parallel to the surface of the imaged area of V1. It is noteworthy that over the course of the experiment the imaged surface of V1 becomes relatively flat under the combination of the cover glass and the gel-like layer of 1% agarose in saline. Finally, the V1 piece was placed on a slide in a petri dish in 0.1 M phosphate buffer or buffer plus fixative with 30% sucrose added. The cover of the petri dish was placed over the piece of brain and weighted with small weights (ca. 100 g). This process does not cause much distortion. These “flattened” pieces were frozen and cut tangentially with the surface vasculature preserved in the first 100– to 150- μ m section. The remaining tissue was sectioned at 52 μ m.

Sections were stained for CO according to methods described previously (Boyd and Matsubara 1996). During cutting, a pin was used to make 3–4 holes at the periphery of the tissue piece. These holes were used as additional aids in section alignment.

All sections were photographed using a Nikon microscope with a $\times 0.5$ objective lens and digital camera. The first section contained visible surface blood vessels. Those vessels were found and marked (see Fig. 2A,B). Similarly, reference images, taken during optical imaging, showed surface blood vessels visible to the camera. These also were marked (Fig. 2D,E). Using these blood vessel marks, the first section was aligned to the reference image (Fig. 2C). Because reference images and data images were taken from exactly the same camera position, simple alignment of the data images to the reference images ensured a near perfect alignment of the data images with the histological landmarks (such as the vertical meridian shown in Fig. 2F). The remaining histological sections were aligned to the first section using the pinholes

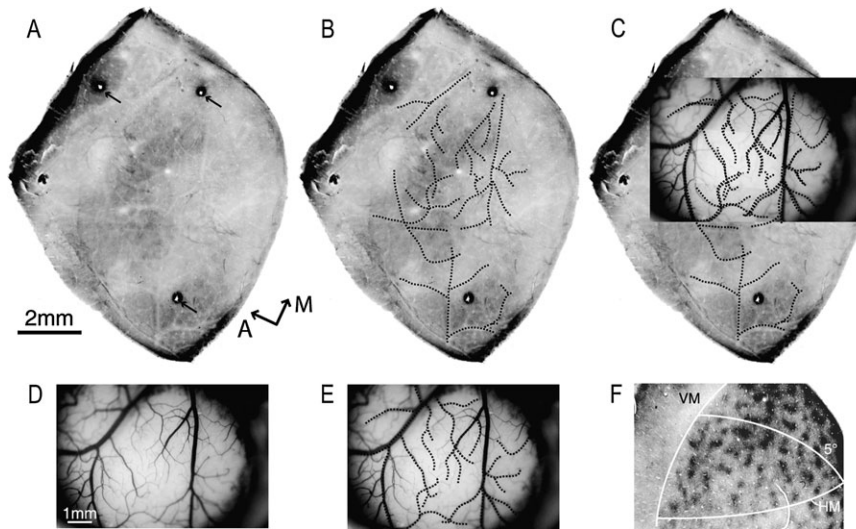


Figure 2. Histological alignment and activation from 1 case (06-07). For this image in color format, please see Supplementary Figure 1. (A) A photomicrograph of the first CO-stained histological section was taken and blood vessels identified. During cutting, a pin was used to make holes perpendicular to the surface for further alignment of the sections (3 small black arrows). A, anterior; M, medial. (B) Major blood vessels were identified and outlined (dotted lines). In cases where there was difficulty assigning a particular vessel branch to a specific larger vessel, a digital color photo taken during the experiment was consulted; however, all blood vessels used to align histology with imaging data were outlined on the first section. (C) Using blood vessels identified in (A, E), a low power reference image (D) was aligned to the first section shown in (A). All alignment is done with the only adjustments being rotation and proportional scaling. (D) A reference image was always taken by the imaging camera just before start of the data acquisition (see Methods). Because the camera was not moved, this reference image remained aligned to the subsequent data images. (E) Blood vessels were identified in the reference image (thin black lines) and were used for aligning the histological data to the imaging data. (F) CO-stained section of cortex, showing major retinotopic landmarks obtained using retinotopically limited stimuli. HM, horizontal meridian. VM, vertical meridian. The 5° line = eccentricity. See text for details.

and tangential blood vessels. The only transformations used in this alignment procedure were rotations and proportional scaling, both applied only to the histological frames and not to any reference images or data image frames.

Optical Imaging

All data were gathered using the Optical Imager 2001 (Optical Imaging Inc, Mountainside, NJ) using methods similar to those described in previous publications (Bosking et al. 1997; Xu, Bosking, et al. 2004; Xu et al. 2005, 2007). In brief, the setup consisted of a differential amplifier, a CCD camera with tandem lens microscope (Ratzlaff and Grinvald 1991), 2 PC computers, and a constant light source with interchangeable filters. The interface to the system was provided through the first PC running the Optical Imaging software. The second PC was used for stimulus presentation with custom code written in MATLAB (Mathworks, Natick, MA) to drive a stimulus generator (Cambridge Research Systems, Rochester, UK). Stimuli were displayed on a 21-inch video monitor (Sony FD Trinitron, model GDM-F400, Sony, Tokyo, Japan) in 120-Hz noninterlaced mode and at a mean luminance of 30 cd/m². The monitor screen maximally subtended approximately 54 × 74° of visual stimulation at a distance of 28.5 cm. The microscope consisted of 2 front-to-front tandem Nikon lenses: 50/50 mm or 50/135 mm. The image was focused just below the cortical surface, and the diaphragm was closed by 1 or 2 f-stops. The light source was filtered at either 540 or 611 nm, with the former used to acquire a reference image of the surface vasculature and the latter used to collect functional data.

Several types of visual stimuli were used. To confirm the placement of the opening, a full-field 100% contrast grating (0.5 c/deg fundamental spatial frequency) was presented at 4 orientations and moved back and forth at 2 Hz. To determine the location of central vision in V1, topographically restricted grating stimuli were presented at 2 orientations in small circular windows (2–5° in diameter), narrow rectangular windows (2° wide), or rings of various widths placed at different locations in the visual field (for details, see Xu et al. 2005). These stimuli allowed us to determine the retinotopic organization and extent of the imaged brain area as shown in Figure 2F.

To study temporal frequency tuning, full-screen square-wave gratings of 0.5 c/deg fundamental spatial frequency at 4 different orientations

and 20% duty cycle were used. These stimuli were selected because, in our previous studies (Xu et al. 2005, 2007), this combination of stimulus attributes proved to be very effective in activating bushy V1. To examine temporal frequency preference maps, 4 frequencies were used: 1, 2, 5, or 10 Hz. These temporal frequencies were chosen based on our previous electrophysiological experiments in V1 of bushy baby (Bonds et al. 1987; DeBruyn et al. 1993). Each experiment consisted of 16 conditions, 4 orientations and 4 temporal frequencies. In 1 animal, we also imaged at higher temporal frequencies (15 and 20 Hz) because V1 in this animal seemed to respond well above 10 Hz. In 1 additional animal, we used sine-wave grating stimuli at the same temporal frequencies, 0.5 c/deg spatial frequency, and 50% contrast. These stimuli were used to examine whether the higher harmonic spatial frequencies inherent in our square-wave gratings could have influenced the results. All stimulus sequences consisted of the following: 5 s of uniform gray screen of mean luminance followed by 8 s of a drifting grating, followed by 12 or 17 s of the same uniform gray screen. Each orientation and temporal frequency was pseudorandomly repeated 10 to 30 times.

The Optical Imaging System stores data in proprietary data files. Before each block of stimuli, consisting of a single repetition of each type of stimulus, the camera records a single reference image for 4 s. This reference image is then automatically subtracted from all consequent frames and the residual amplified. Both the reference frame (frame zero) and amplification parameters are stored in a file header. During stimulus presentation, the camera collects 30 frames/s, and these 30 frames are automatically summed into a single data frame. Therefore, each stimulus condition of 25–30 s produces 25–30 differential data frames.

Analysis

Reconstructed raw data (referred to here as raw data) were obtained by reversing the steps done by the Optical Imaging algorithm described above (Optical Imaging, personal communication). All quantitative analyses were performed on reconstructed raw data. To add certainty to our conclusions, we performed a number of quantitative comparisons. Because some of these are new to the optical imaging literature, we have provided more details in the relevant subsections of the Results.

The first step in our analysis was the conversion of raw frames into baseline normalized frames as described in Siegel et al. (2003). In brief, each reconstructed raw file consisted of a zero reference frame and 25–30 data frames, with frames 6–14 corresponding to the grating presentation and frames 1–5 corresponding to presentation of an equiluminant gray screen. The zero reference images from all trials were averaged, their means and standard deviations (SDs) were determined, and all pixels that had values higher than the mean plus half a SD were selected as a region of interest (ROI). Frames 6–14 of each trial and condition were averaged and divided by the average of the first 5 frames, producing baseline normalized images. The means and SDs of the pixels within the ROI from the baseline normalized images were determined, producing a mean-SD pair value for each frame. An automatic rejection procedure was used which removed all the frames whose means were more than 2 SDs away from the population's average mean or whose SDs were more than 3 interquartile intervals away from the population's median SD (Siegel et al. 2003). The remaining baseline normalized frames were averaged separately for each condition, producing 16 baseline normalized images, 1 for each orientation and temporal frequency. Before doing any quantitative analysis for each data set, a binary mask was created in which bone and large blood vessels that show up in the baseline normalized images were marked as zero.

The next step involved obtaining the single-condition images (Fig. 4). Nonuniform bias due to cortical curvature (direct-coupled shifts) was removed by convolving each image with a Gaussian kernel with sigma of 1.0 mm and subtracting the result from the original image (Bosking et al. 1997; Xu, Bosking, et al. 2004).

We employed multiple qualitative and quantitative methods to test our hypotheses. The details of these methods are included with the relevant results presented below. The main distinction between our different hypotheses concerned the position of the activation areas relative to each other when different combinations of temporal frequencies and orientations were presented (see Fig. 1). Therefore, we needed to show whether individual activation domains at single orientation and different temporal frequencies moved in relation to each other as temporal frequencies were changed and, if so, to determine the nature of that movement. We accomplished this by cross-correlating sample regions from single-condition images, determining the precise positions of each individual activation domain in all conditions, comparing their respective positions, and performing similarity analysis across conditions (see below). Finally, we quantified the strength of the response at different temporal frequencies using a curve fitting technique.

To determine the signal strength for each pixel at each temporal frequency, we linearly fit the data, consisting of single-condition images without low-pass filtering, to the following equation:

$$R_{I,J,v}(\theta) = a_{I,J,v} \times \sin(\theta) + b_{I,J,v} \times \cos(\theta) + c_{I,J,v}, \quad (1)$$

where $R_{I,J,v}(\theta)$ is the reflectance of (I,J) pixel for temporal frequency, v (4 conditions), as a function of orientation θ (4 orientations). Each temporal frequency and pixel was analyzed independently. For a given pixel, the preferred angle is

$$\Phi_{I,J,v} = \arctan(a_{I,J,v}/b_{I,J,v}), \quad (2)$$

with appropriate quadrant correction, and the pixel's maximum response at a given temporal frequency is

$$M_{I,J,v} = \sqrt{a_{I,J,v}^2 + b_{I,J,v}^2}. \quad (3)$$

This analysis produced preferred orientation and magnitude of response maps for each temporal frequency (Fig. 3). Preferred orientation map pixels were divided into 8 groups with the mean strength in each group obtained from maps of the magnitudes of response (Figs 12 and 14). To simplify comparisons between cases, the average of the strongest response across all 4 temporal frequencies was set to unity. To determine if the differences in response magnitude were significant, a 2-way analysis of variance with a subsequent Tukey honestly significant difference test was run in MATLAB on all mean response values.

We also were interested in whether there was a difference in temporal frequency preference in CO blob as opposed to interblob regions of V1. To map the appropriate ROIs, we low-pass filtered

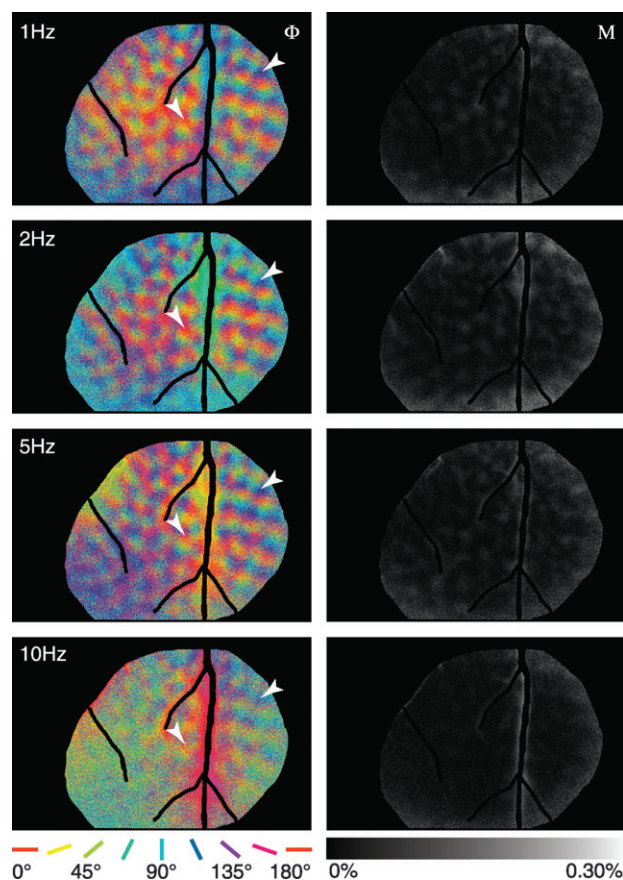


Figure 3. Pixel-wise linear fit. Preferred orientation maps (Φ) at 4 temporal frequencies (left column). Magnitude maps (M) (right column). Colors refer to the preferred orientations and the gray scale to the response magnitude relative to baseline as determined by linear fit. White arrowheads in the left column show that at different temporal frequencies, orientation preference at a given location does not change. See Methods for details (case 06-07lo).

images taken of the histological sections with a 50- μ m filter averaging kernel and subtracted the background obtained with a 500- μ m filter averaging kernel. The resulting images were then thresholded into 3 roughly equal groups according to pixel brightness (Fig. 13). The darkest third of the pixels were assigned to CO blobs and the brightest third to interblobs (Boyd and Casagrande 1999; Xu et al. 2005). Visual inspection was used to confirm that all the regions of the cortex that were imaged were assigned to the correct compartment. We aligned these maps with activity maps as described above, which allowed us to repeat the strength calculations segmented by pixels within CO blob regions or interblob regions.

Results

We first describe our findings using spatially restricted stimuli to define retinotopic regions in V1. Next, we demonstrate the overall organization of temporal frequency selectivity. Our results support the third hypothesis (Fig. 1C). Unlike spatial frequencies, temporal frequencies are not clustered in modules. Instead, all temporal frequencies are represented at each spatial location with no obvious shifts in preferences across the parts of V1 representing the central 10–15° of visual space. We then show that global measures of temporal frequency preference measured using optical imaging match closely with measures reported for single cells in V1 (DeBruyn et al. 1993).

Finally, we describe results comparing the distribution of temporal frequencies across CO compartments. These results do not support previous results suggesting that there is a difference in optimal temporal frequency selectivity between CO blob and interblob regions.

Mapping V1 and Aligning Images

All our reported results were collected from area V1 within the representation of the central 15° of visual space confirmed using visuotopically restricted stimuli and histology (see Methods). Figure 2F shows the representation of the horizontal and vertical meridians (HM and VM lines) based on cortical activation produced by using 2° rectangular windows presented either on the HM or VM. Note that the intersection of these lines defines the center of gaze or the *area centralis* representation. For this case, approximately 8–10° of visual space was within view of the camera on the dorsal surface of V1. In the other 6 cases, slightly different openings were made, but all allowed us to image the representation of approximately the central 10–15° of visual space. In all reported cases, we had robust responses to optimal full-field gratings. Two different lens arrangements were used in our experiments; the 50/50 mm lens combination provided an 87 pixels/mm (11.5 μm) level of resolution, whereas the 50/135 mm lens combination produced a 235 pixels/mm (4.26 μm) level of resolution (Figs 4 and 13D). At both resolutions, we saw very strong activation of cortex with clearly defined orientation domains. It is important also to keep in mind, however, that optical imaging can only sample the supragranular layers of cortex and is not able to sample the functional organization of cortex much below approximately 500 μm of cortex, corresponding to the supragranular layers (Bonhoeffer and Grinvald 1993). Therefore, when interpreting our data, as well as any optical imaging

data, it is important to keep in mind that the structure of the functional maps could differ in the lower layers.

Linear Fitting of the Orientation Data

Baseline normalized single-condition response data were organized into single temporal frequency groups and fitted using Equation (1). Resultant orientation preference images (Fig. 3 left column) were similar at all tested temporal frequencies with the only difference being that there was less activation for all orientations at 10 Hz than at lower temporal frequencies (Fig. 3 right column). This can be appreciated visually by examination of common activation points (arrows). The same general pattern, in which activation domains at different temporal frequencies and same orientation appeared to be in the same place, was evident in single-condition images at both low and high power (Fig. 4).

Responses at Different Temporal Frequencies

Figure 4 shows activation patterns seen in V1 in 3 different cases in response to moving gratings shown at 4 different temporal frequencies (1, 2, 5, and 10 Hz). These images are single-condition maps baseline normalized by the first 5 gray (blank screen) frames. Because all the images in this figure were normalized to the same range, the strength of response was roughly proportional to the contrast seen, with darker regions showing stronger responses and lighter areas—weak or no response. Animals showed some individual variability in the degree of sensitivity to higher temporal frequency stimulation.

For example, in Figure 4, case 06-07hi, all 4 temporal frequencies produced activation up to 10 Hz (far right panel). In case 05-05 (Fig. 4), the response at 10 Hz was weaker making it virtually impossible to distinguish areas of activation from surrounding nonresponding regions. Still, quantification

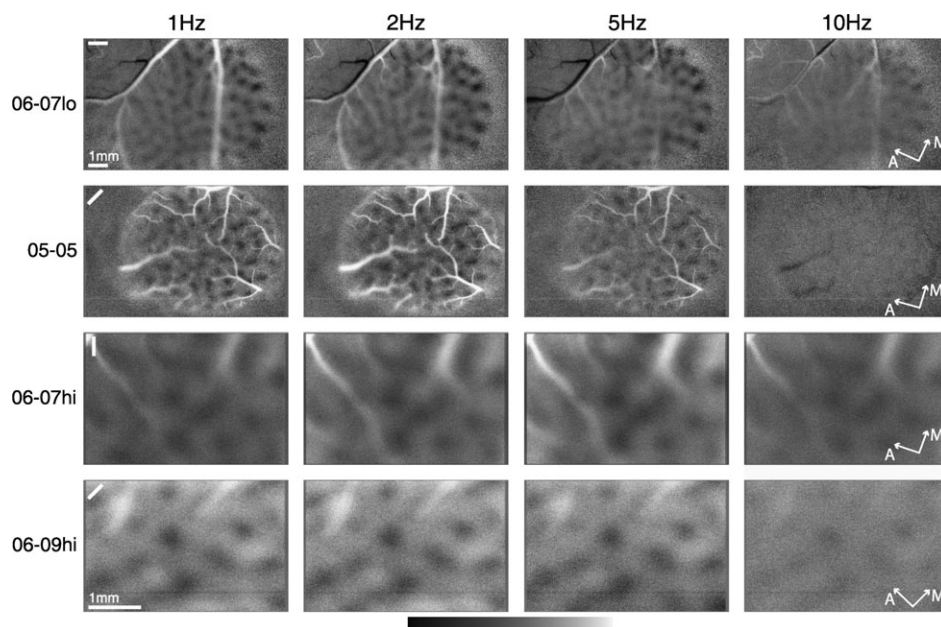


Figure 4. Single-condition activation patterns. All images are single-condition images normalized to the first 5 (blank) frames as described in Methods. Each column represents responses at the indicated temporal frequency. Each row shows the response to the indicated orientation (upper left corner of each image) in a separate case, case number indicated to the left. These images show reduction in the strength of the response with increases in temporal frequency of the stimuli. Darker areas represent stronger responses. The first 2 rows are low magnification (lo) and last 2 rows are high magnification (hi) images. The grayscale bar indicates range of response relative to baseline as follows: 06-07lo (−0.34% to 0.42%), 05-05 (−0.17% to 0.38%), 06-07hi (−0.22% to 0.12%), and 06-09hi (−0.09% to 0.12%). Cases (05-05, 06-07, and 06-09). A, anterior; M, medial.

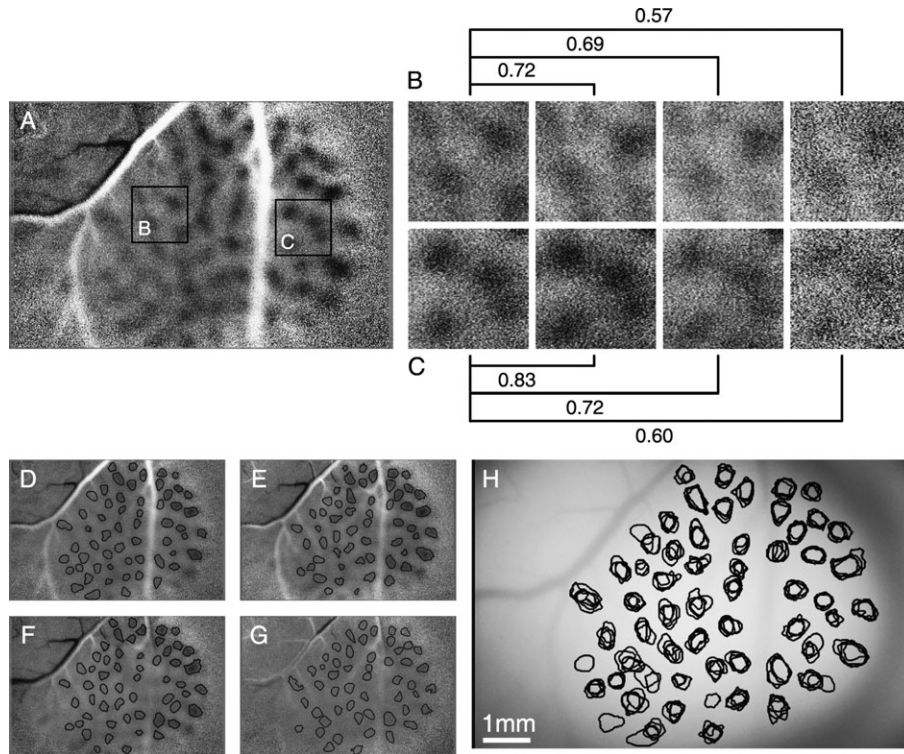


Figure 5. Analysis of low magnification single-condition maps at different temporal frequencies (case 06-07). For this image in color format, please see Supplementary Figure 2. Panel (A) shows the same region as is shown in Figure 4 at higher contrast. Within panel A, 2 ROIs designated B and C in enclosed boxes on the image itself were selected. These are shown enlarged in the 4 panel sets designated (B) and (C) to the right. In (B) and (C), activation (dark patches) at 4 temporal frequencies (1, 2, 5, and 10 Hz left to right) are shown for these ROIs. The connecting lines and numbers above the images are correlations for the corresponding images (see text for detailed description). (D–G) show the outlines of each area of activation in the entire imaged area shown in (A) at the 4 temporal frequencies (D): 1 Hz, (E): 2 Hz, (F): 5 Hz, (G): 10 Hz. H. The same outlines as shown in (D–G) superimposed on the reference image. See text for details.

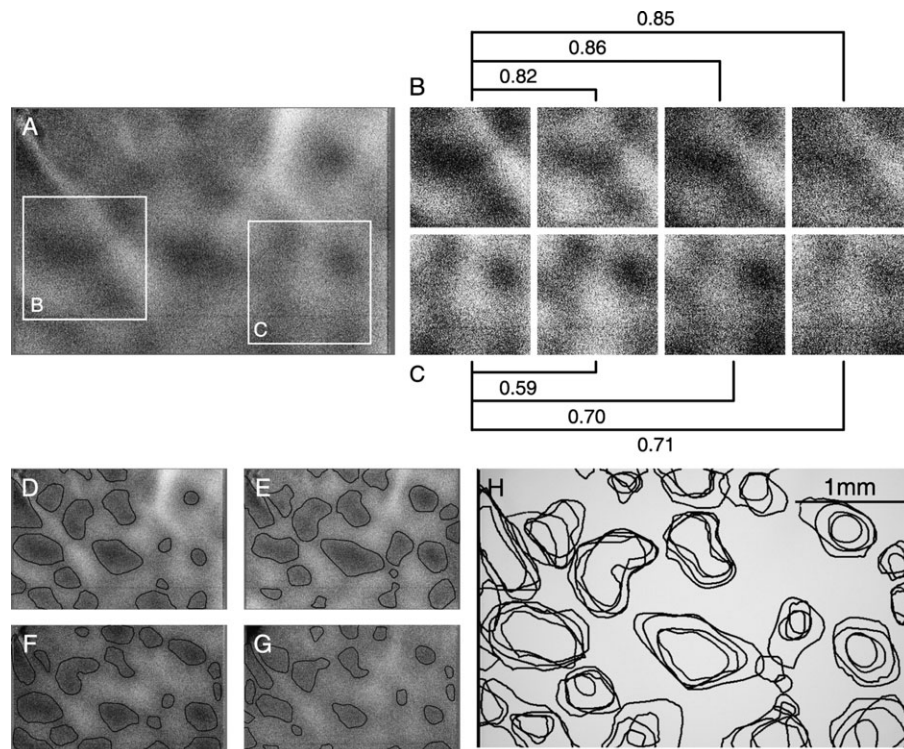


Figure 6. Analysis of high magnification single-condition maps at different temporal frequencies (case 06-07). For this image in color format, please see Supplementary Figure 3. Same analysis as was performed for Figure 5 was done on high magnification images. All conventions are as in Figure 5.

of individual pixels suggested that activation was above background. In all cases, the strongest responses were seen at the lower temporal frequencies (1 and 2 Hz) with a peak at 2 Hz. Careful examination of the different maps of activation at different frequencies suggested qualitatively that they overlapped with little variation. Small differences in the appearance of individual activation domains were only visible at the edges of the craniotomy and along the course of medium sized blood vessels. These blood vessels also tended to have an inconsistent appearance across conditions (blood vessels generally do change appearance at the same time as cortical tissue around them and are affected more than cortical tissue by minor changes in physiology). Therefore, our main result was that there were no major changes in the geometric structure of the single-condition maps across temporal frequencies, such as changes in domain size or number. This is an important qualitative observation in light of our predictions (see Fig. 1).

Structure of Single-Condition Maps at Different Temporal Frequencies

To test whether regions of imaged cortex preferring the same temporal frequency were clustered, we used single-condition images at different temporal frequencies. Figures 5 and 6 compare the relationship of single-condition orientation domains at different temporal frequencies. Initially, we chose 2 representative ROIs in the single-conditions maps, free of blood vessels and centrally located, smoothed these ROIs using a 2×2 pixel ($23 \times 23 \mu\text{m}$) kernel, and determined their similarities using cross correlations. The contrast in these images was increased to make signal comparisons easier. The sample ROIs at both magnifications were compared visually and quantitatively. Both figures show that the shape, position, and size of the activation regions (darker areas) are similar at all 4 temporal frequencies.

At low magnification (Fig. 5A-C), we found that ROIs indicated by letters in Figure 5 at 1 Hz (Fig. 5B,C) were well correlated with the same regions at 2, 5, and 10 Hz with correlation coefficients of 0.72 (0.83), 0.69 (0.72), and 0.57 (0.60) (numbers in parenthesis represent correlation coefficients for region B), respectively. To distinguish from a random organization, the ROIs taken at 1-Hz temporal frequency were rotated 180° . When this was done, correlation coefficients dropped to 0.02 (0.53), 0.08 (0.40), and 0.04 (0.44), respectively, for these same regions. The same analysis was repeated on images collected at high magnification (Fig. 6A-C).

Once again, we obtained high correlation coefficients of 0.82 (0.59), 0.86 (0.70), and 0.85 (0.71). For comparison, the “random” 180° rotated images at 1 Hz yielded correlation coefficients of 0.28 (0.17), 0.48 (-0.19), and 0.39 (-0.15). The high correlations between images at different temporal frequencies are not consistent with either the first or second predictions described in the Introduction (Fig. 1). Analysis of data from all the other cases showed the same result.

As a second approach to the question of stability of patches with varying temporal frequency of the stimuli, outlines of orientation domains were generated. The outlines of these orientation domains were compared as follows (Figs 5 and 6D-H). First, to reduce the high spatial frequency noise, each image was convolved with a $57\text{-}\mu\text{m}$ averaging kernel. Next in Adobe Photoshop (Adobe Systems Inc, San Jose, CA), a binary threshold function was employed so that only approximately 30% darkest pixels were selected in each image. The 30% cutoff was selected for consistency with our previous studies (Xu, Bosking, et al. 2004; Xu et al. 2005) and to provide a conservative estimate of the areas of activation. Finally, obvious noise artifacts and regions containing blood vessels were excluded. The resulting images were aligned in a stack to determine if any spatial shifts of orientation domains occurred that correlated with different temporal frequencies.

The patch locations, representing activation domains at different temporal frequencies, overlapped (Figs 5D-H and 6D-H, low and high magnification). These results again reinforced the point that the overall structure of single-condition temporal frequency preference maps does not change with temporal frequency of the stimuli. In fact, Figures 5H and 6H demonstrate that the majority of domains at different temporal frequencies were aligned almost perfectly with each other; nevertheless, there were always slight variations. At low magnification (Fig. 5H), there were a few slightly misaligned domains or even an occasional nonmatched domain, which likely resulted from increased noise at those locales because there was no consistency in the pattern. There also were a few misaligned domains at higher magnification (Fig. 6H). Additionally, at high magnification, we saw changes in sizes of activation domains at different temporal frequencies but most of these domains overlapped completely which does not support hypothesis 2 (Fig. 1), which predicts that activation domains at different temporal frequencies never overlap completely. In Figure 6H, the majority of domains totally overlap and, in fact, the 10 Hz domains are often located

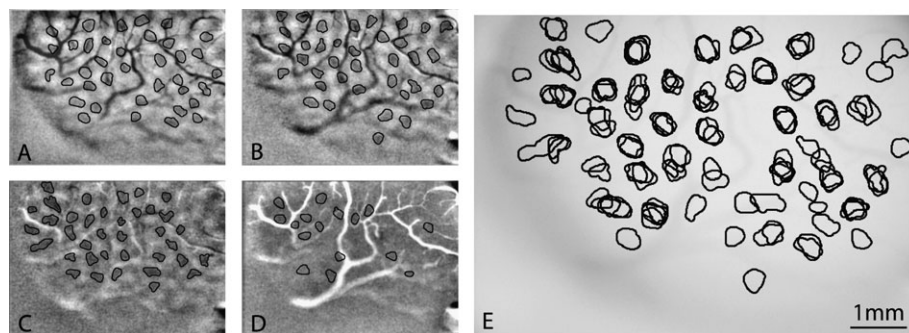


Figure 7. Differential images at different temporal frequencies acquired using sine-wave gratings. For this image in color format, please see Supplementary Figure 4. (A-D) show responses at 4 temporal frequencies. (A) 1 Hz, (B) 2 Hz, (C) 5 Hz, and (D) 10 Hz. Contrast was enhanced by clipping to 2 SD. (E) The outlines of activation domains are the same as shown in (A-D) superimposed on the reference image. See text for details.

completely inside activation domains produced by lower preferred temporal frequencies. The most likely conclusion from this result is that the size differences seen were the result of an “iceberg” effect, produced by decreasing signal at nonpreferred frequencies; therefore, the data so far are consistent with the idea that different temporal frequencies are not represented as separate domains in V1. Additional quantification using a center-of-gravity computation is provided below, which supports this preliminary conclusion.

Structure of Differential Maps at Different Temporal Frequencies Using Sine-Wave Gratings

In all our experiments, we used drifting square-wave gratings as stimuli. Given that square-wave gratings contain a fundamental spatial frequency and the higher harmonics, we thought it important to test our conclusions using sine-wave gratings presented at 2 orientations and all 4 temporal frequencies. The results are shown in Figure 7, with the only difference being that the images used in this analysis were differential images, obtained by dividing baseline normalized images from the 0° grating presentations by similar images from the 90° grating presentations. The images shown in Figure 7A–D were clipped at 2 SDs from the mean pixel value in the image. The domains activated by different temporal frequencies were outlined as described for Figures 5 and 6 (see Methods for details). The most significant difference between the responses to square- and sine-wave grating stimuli was a decrease in overall activation, as was expected from the decreased contrast in our sine-wave stimuli (see Methods and Xu et al. 2007). Additionally, blood vessel artifacts become more pronounced in the differential image. These 2 factors contribute to the differences in number and location of the domains. Nevertheless, the results, shown in Figure 7E, demonstrate that even with a single spatial frequency different temporal frequencies activated the same locations in cortex. At 10 Hz, due to very low response magnitude, the thresholding process yielded fewer activation domains, but the observed domains still were qualitatively aligned with domains activated at lower temporal frequencies.

Quantification of Center of Mass Locations

Our results so far have been inconsistent with our first hypothesis (Fig. 1A) which states that orientation and temporal frequency preference are interdependent. Next, we examined whether temporal frequency preference is mapped into domains similar to those found for spatial frequency (Xu et al. 2007). A commercially available image quantification software package (Image Processing Tool kit v.5, Reindeer Graphics, Asheville, NC) was used to determine the location of centers of mass of the activation domains shown in Figures 5 and 6D–H. The computed nearest neighbor distances between the centers of mass across different temporal frequencies are shown in Figure 8A,B. On average, a single activation domain had the equivalent diameter, that is the diameter of a circle of the same total area, $298 \pm 64 \mu\text{m}$ (SD, $N = 770$). The nearest neighbor distance of the activation domains at 1 temporal frequency was $544 \pm 112 \mu\text{m}$ (SD, $N = 770$). The nearest neighbor distance of the centers of activation at different temporal frequencies was $53 \pm 74 \mu\text{m}$ (SD, $N = 201$) (median = $32 \mu\text{m}$ and interquartile range [range from 25th to 75th percentile] = $40 \mu\text{m}$) (Fig. 8C). These results support hypothesis

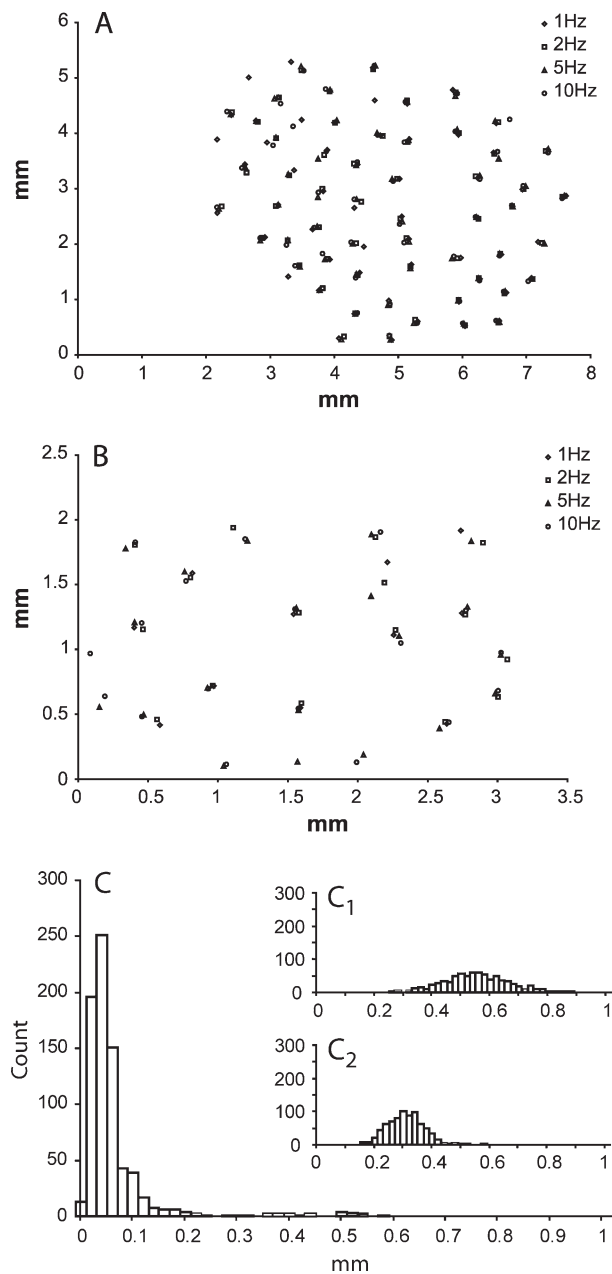


Figure 8. Locations of centers of mass of domains identified in Figures 5 and 6. For this image in color format, please see Supplementary Figure 5. (A, B) are locations of centers of mass of the activation domains outlined in Figures 5 and 6, respectively. Centers of mass are shown in real topographic coordinates. Symbols indicate centers of mass at 4 temporal frequencies: 1 Hz–diamond, 2 Hz–square, 5 Hz–triangle, and 10 Hz–circle. (C) Distribution of the nearest neighbor distances of centers of mass of activation domains at same orientation and different temporal frequencies, as in panel (A). Inset C₁ depicts the distribution of nearest neighbor distances of centers of mass at the single temporal frequency and orientation. Inset C₂ depicts distribution of equivalent diameters of activation domains.

3 which predicts that the distance between the centers of mass should be close to zero, indicating extensive overlap.

Invariance of Orientation Domains with Respect to Temporal Frequency Changes

In order to quantify the shifts in the activation domains with different temporal frequencies in a manner independent of the centroid analysis, 2 further tests were employed. First, each

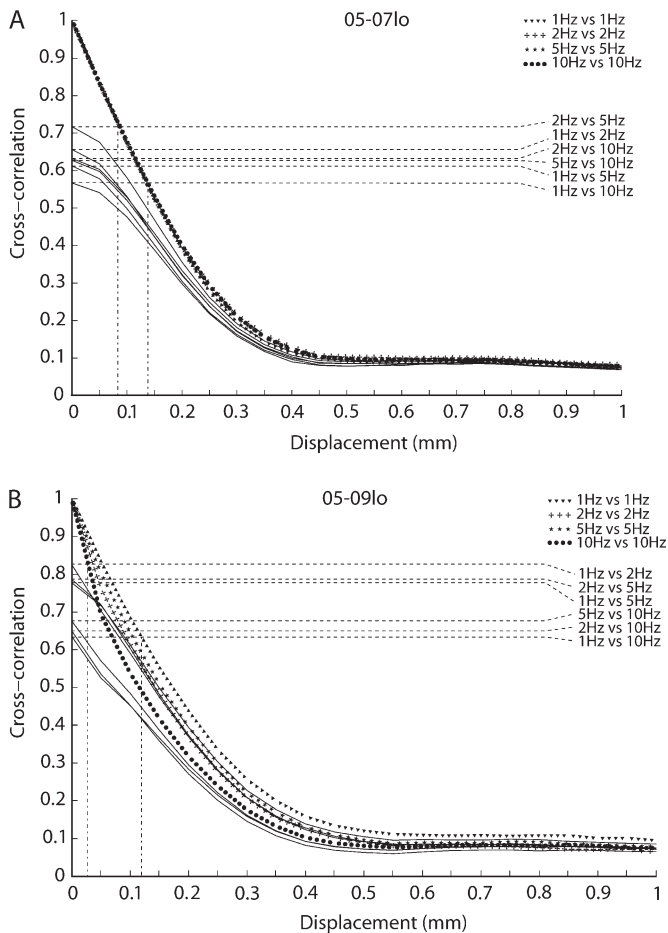


Figure 9. Cross-correlation coefficient as a function of independent random shift of activation domains. For this image in color format, please see Supplementary Figure 6. (A, B) are graphs of correlation coefficients obtained by running cross-correlations between images corresponding to responses to different temporal frequencies at the same orientation, with and without random independent shifts of individual domains. (A) Graph of coefficient of change in a case in which activation domains were obtained by thresholding single-condition images at the 30% darkest pixels. (B) Similar to (A), except domains in individual images were obtained by automatic thresholding of Z-normalized images. The symbols corresponding to individual temporal frequencies are indicated in the legends in upper right corner of each panel. Only domains in the image corresponding to the second temporal frequency were independently shifted by indicated distance. The horizontal dotted lines indicate correlation levels of the images corresponding to different temporal frequencies without shift. Two vertical dotted lines indicate the equivalent random shift of the domains that would produce the same level of correlation as is seen between images of activation domains at different temporal frequencies.

image at a single temporal frequency was thresholded at 30% darkest pixels and obvious artifacts removed, as described above. Then, each image was processed separately to identify and label each of the domains as contiguous thresholded regions. Each of these domains was placed into a separate image. Thus, each image at a single temporal frequency provided 20–60 images. Cross-correlations were then computed between domains at each temporal frequency in the original set (0 mm displacement) and again after randomly shifting domains from 50 to 1000 μm from their original location in 50- μm steps (Fig. 9A).

Second, the same analysis was run on data in which activation domains were outlined automatically as follows. The Z-normalized single-condition images were thresholded at

a 0.4–0.5 SD level (Fig. 12). The cross-correlations between activation domains at different temporal frequencies were then computed with and without randomly shifting the locations of these activation domains (Fig. 9B).

The cross-correlations between domains at different temporal frequencies at a fixed orientation were in the range of 0.57–0.82 (Fig. 9). The results of the analysis on the manual and automatically thresholded data were similar (Fig. 9). To achieve the level of correlation observed between the images at different temporal frequencies, domains in the original data can be randomly moved by no more than 25–140 μm . This is less than 1 half of the equivalent diameter of an activation domain ($298 \pm 64 \mu\text{m}$ as calculated above). For comparison, cross-correlations between images of activation produced by different orientations lie in the range of -0.06 – 0.31 (data not shown). Taken together with the above analyses, these additional comparisons indicate that domain locations are reproducible across temporal frequencies within 25–140 μm . This finding supports our third hypothesis (Fig. 1), which predicts that activation domains must have extensive overlap at different temporal frequencies.

Automatic Classification of Z-Normalized Images

As a third test of domain stability across temporal frequencies we used a hierarchical tree clustering analysis (Duda et al. 2001). This analysis was done on the z-normalized images using an automated classification algorithm. This analysis, without any *a priori* assumptions, determines the similarity of 2 or more images. In this analysis each image becomes a point in $N \times M$ dimensional space, where N and M are the dimensions of an individual image in pixels, and distances between those data points is calculated, using a furthest neighbor algorithm. These distances were used to cluster the images into a hierarchical tree (dendrogram) (Duda et al. 2001), in which the lowest branches are singleton clusters of the original data and the length of the connecting branches indicates the closeness of the linked images. The more similar the images are, the closer they will be on a hierarchical tree.

This analysis reliably showed that the 16 conditions can be consistently and reliably classified into 4 orientation groups (Fig. 10 is an example). In other words, in this $N \times M$ dimensional space, images of responses to stimuli at different temporal frequencies at a given orientation are much closer to each other than are images of responses to the stimuli at different orientations at a given temporal frequency. This is further support that the domain location is independent of temporal frequency.

Absence of Visible Temporal Frequency Preference Domains

Previous analyses demonstrated little support for the first or second hypothesis in Figure 1; however, there still could exist a possibility that temporal frequency preference is organized into domains similar to orientation and spatial frequency preference domains in bush babies (Xu et al. 2005, 2007) and that they could not be identified due to the strength of the orientation data. To eliminate the possibility of missing temporal frequency preference domains located within orientation preference domains, we averaged our 16 baseline normalized single-condition images either along the orientation dimension or along the temporal frequency dimension, thus

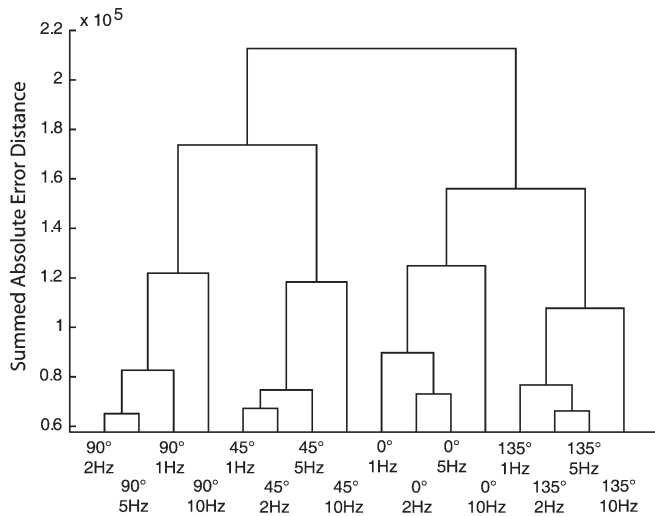


Figure 10. Dendrogram showing similarity between 16 Z-normalized conditions. This dendrogram was obtained by determining the distance between pairs of images using summed-absolute-error (SAE) distance metrics (see Methods and text for details). The lowest branches represent individual images. The length of linking branches indicates similarity between linked images. The y-axis is the SAE distance.

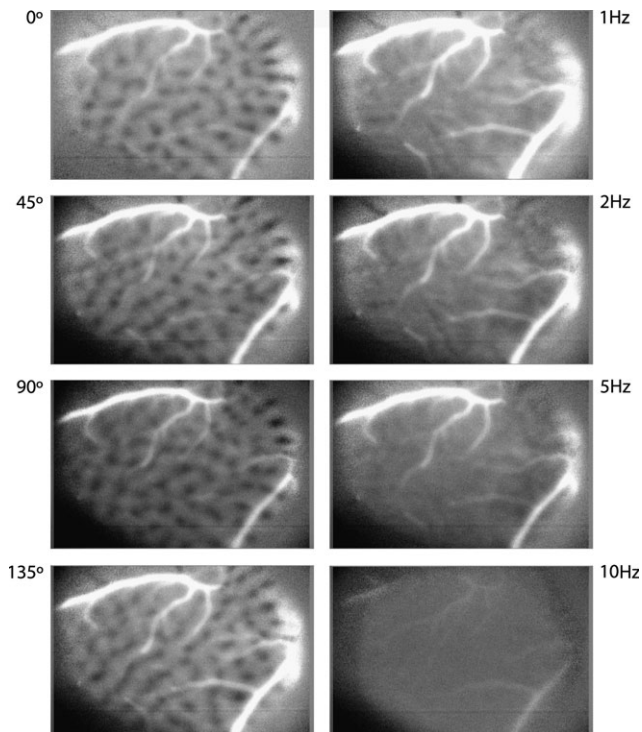


Figure 11. Orientation and temporal frequency preference images. In an attempt to isolate pure orientation and pure temporal frequency responses, 16 single-condition images were averaged along temporal frequency or orientation dimension. Left column are responses to 4 orientations with temporal frequencies averaged out. Right column are responses to 4 temporal frequencies with orientations averaged out.

producing 8 images in which either the influence of orientation or of temporal frequency was removed (4 images that had temporal frequency averaged out and 4 images in which orientation was averaged out, Fig. 11, left and right columns,

respectively). There were very strong orientation domains in the absence of temporal frequency influence; there were no visible domains in the absence of orientation influence (to see how these averaged orientation preference domains align to the orientation domains in Fig. 5, see Supplementary Fig. 8). This is an important finding because the same type of analysis clearly demonstrated the existence of spatial frequency domains in bush baby V1 (Xu et al. 2007). Therefore, we conclude that our data support the third hypothesis (Fig. 1), stating that temporal frequency preference is distributed uniformly across V1 cortex without any significant clustering.

Quantification of Response Strength at Different Temporal Frequencies

The next analysis was to quantify the relative strength of response at different temporal frequencies and orientations. To reduce noise, the responses at each pixel of baseline normalized images were fit to a sinusoid, separately for each temporal frequency (Fig. 3). The regressions produced 2 sets of data, orientation preference at each pixel location (Fig. 3 left column), and magnitude of maximal response at each pixel location (Fig. 3 right column), for each temporal frequency. Both sets of data were used to determine overall responses at different temporal frequencies (see Methods). Our previous electrophysiological investigations showed that most neurons in bush baby V1 can still respond at 10 Hz, even though the optimal temporal frequency for most cells lies within 1–5 Hz (DeBruyn et al. 1993). All optical imaging cases showed similar results, 3 of which are shown in Figure 12. Imaging at both high and low magnification resulted in the same response profiles at different temporal frequencies. Optical activation was highest at the 2-Hz temporal frequency. The 2-Hz value was then used for normalization of the other temporal frequencies in Figure 12.

Activation magnitudes at 1 and 5 Hz were similar to each other, but about 5–10% lower than those seen at 2 Hz (with $P < 0.01$ in all but 1 case [$N = 7$]). In 4 of the cases, the activation level at 5 Hz was lower than at 1 Hz ($P < 0.01$), as in case 05-05 (0.97 ± 0.02 normalized response units (nr) at 1 Hz vs 0.90 ± 0.002 nr at 5 Hz, mean \pm SE) or case 06-09l o (0.93 ± 0.03 nr vs. 0.89 ± 0.01 nr). As illustrated by comparing high and low magnification results for cases 06-07 and 06-09, however, it is not the absolute magnitude of response at 1 and 5 Hz that is most preserved; rather, it is their relative strength in relationship to the strongest response at 2 Hz. In all cases, responses at the lowest 3 temporal frequencies were on average 10–15% higher than at 10 Hz ($P < 0.01$). Even though the response strength at 10 Hz was the smallest, it was still possible to detect the orientation domains visually in single-condition maps (Figs 4–6). In fact, in 1 case, hints of orientation domains in the differential images were identified even at 20 Hz.

CO Domain Dependence of Temporal Frequency Tuning

The relationship between the CO-defined compartments and temporal frequency selectivity also was examined. Figure 13 depicts a thresholded image of V1. In these images, cortex was segmented into 3 zones based on CO staining intensity: CO blobs (black), CO blob borders (gray), and CO light interblobs (white). All 3 compartments were made to have approximately equal numbers of pixels. These images were superimposed on our optical maps of activation. Using a Monte-Carlo approach, 500 pixels were selected randomly that belonged to either

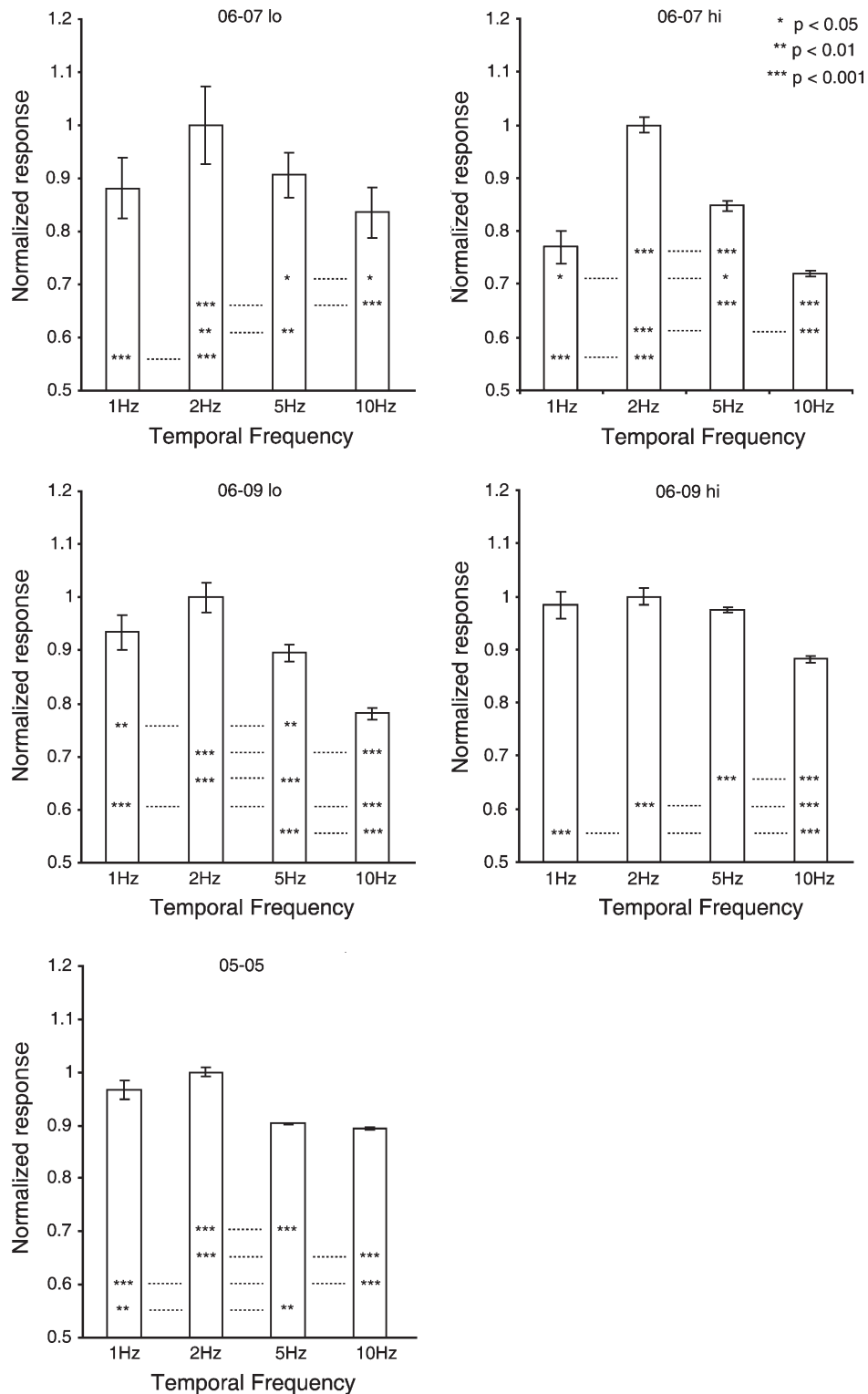


Figure 12. Response strengths at different temporal frequencies. Five representative examples are shown, with case numbers above the graphs. The strongest response in each case was at 2 Hz. All other values were normalized to this value, taken as 1.0. Bars indicate the standard error around the mean. Results of post hoc Tukey honestly significant difference pairwise tests are shown on the graphs with asterisks (* $P < 0.05$, ** $P < 0.01$, *** $P < 0.001$) indicating level of significance. Each pairwise test is shown within an aligned row of asterisks connected by a dotted line. Only combinations that were significantly different are indicated. See text for details.

a blob or an interblob (repeated 50 times with replacement). Then using the magnitude of response maps (Fig. 3 right column), the average strength of response in the respective compartments was determined. A modified Weibull function

was fit to the response data. This allowed us to estimate the maximum temporal frequency preference in both compartments.

As can be seen from Figure 14, there was little difference in the preferred temporal frequency between blob versus

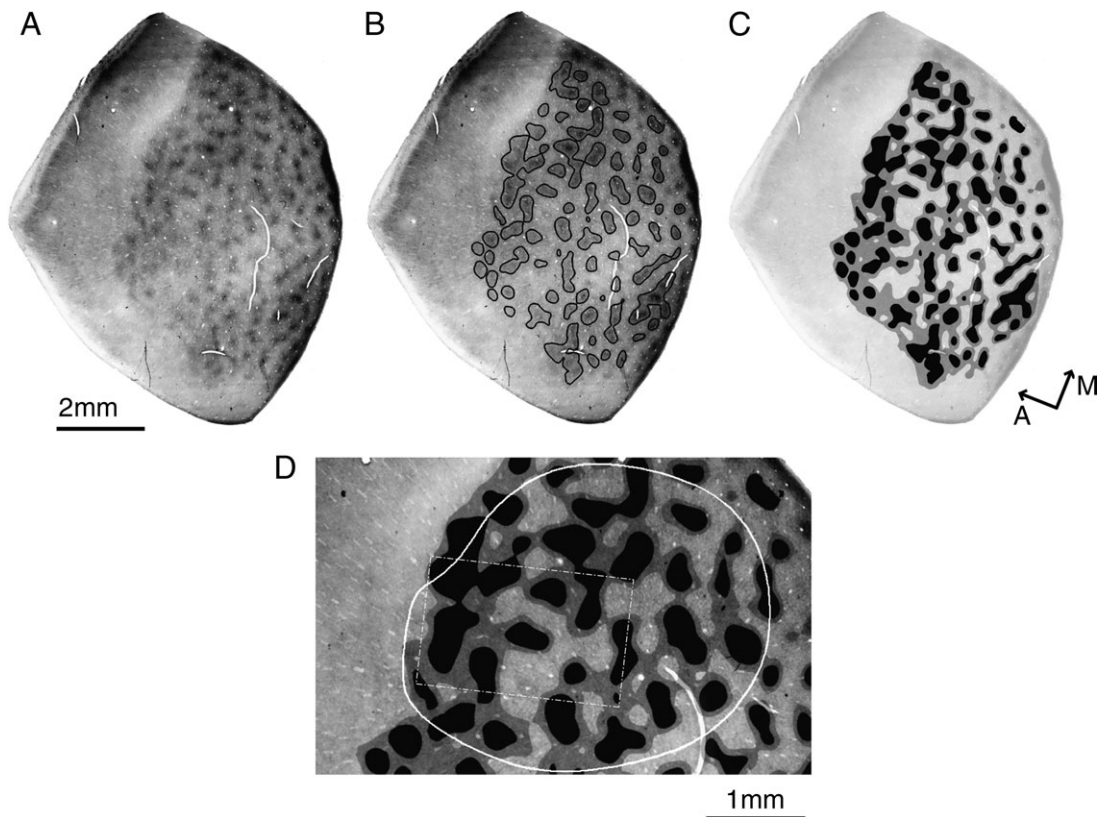


Figure 13. Example of thresholding method to separate CO compartments in V1 (case 06-07). For this image in color format, please see Supplementary Figure 7. (A) CO-stained tangential section. (B) Outlines of CO blob domains. (C) All 3 subdomains, black-CO blobs, gray-border regions, and white-interblobs. Only CO blob and interblob regions were compared for temporal frequency preference content. See text for details. A, anterior; M, medial. (D) Area in (C) within view of our camera at low power. White rectangular outline is the area of the frame imaged by the camera at high power.

interblob compartments. Both areas have maximum responses at about 2 Hz (2.67 ± 0.36 vs. 2.58 ± 0.35 [SD] Hz and 2.06 ± 0.27 vs. 1.99 ± 0.31 Hz for 2 cases presented). The *t*-test demonstrated that there is no significant difference ($P < 0.22$ and $P < 0.17$, respectively) in preferred temporal frequency between the 2 compartments.

Discussion

The primary goal of this study was to determine how temporal frequency selectivity is mapped in V1 of primates using bush babies as a model. We had 3 hypotheses for how temporal frequency selectivity could be organized. The first hypothesis was that orientation tuning depends on temporal frequency tuning and therefore orientation domains should shift with different temporal frequencies. The second hypothesis was that orientation domains do not depend on temporal frequency tuning but different temporal frequencies, like spatial frequencies, cluster into separate domains. This second hypothesis seemed most likely given that spatial frequency is organized this way in bush baby (Xu et al. 2007). Surprisingly, the data supported neither of these hypotheses. Instead, the data were most consistent with our third hypothesis, namely, that orientation does not depend on temporal frequency tuning and that sensitivities to different temporal frequencies do not cluster but are represented uniformly across V1. This result was particularly interesting given that other attribute maps of orientation, ocular dominance, and spatial frequency in the

bush baby are clearly organized into patch-like domains. Because this result was so surprising, we used a range of independent quantitative methods to verify these findings. These methods, some of which have not been applied previously to optical imaging data, all suggest a lack of domains for temporal frequency selectivity and verify the existence of such domains for orientation.

These results suggest either that there is something unique about temporal frequency that requires that it be represented in this way or that only a certain number of variables can be represented as clusters and still achieve adequate coverage. Swindale (2004) has recently addressed some of these issues and pointed out that more binary (ocular dominance) or cyclic (orientation) variables can be organized into domains in V1 while still maintaining coverage than scalar variables such as spatial or temporal frequency. He argues that although 5 or more of binary or cyclic variables can be represented in such a way, only 1 or 2 scalar variables can be represented without creating holes in the retinotopic map. Models of the type he describes would then support the third possibility, namely that 2 scalar variables can not be adequately represented as clusters in bush baby V1.

In the following sections of the Discussion, we first review how well the current optical imaging data in bush baby fit with previous physiological, behavioral, and anatomical results in this species, then compare these results to data reported in other species, and consider the implications of these data for mapping of visual features in general. Finally, we discuss the

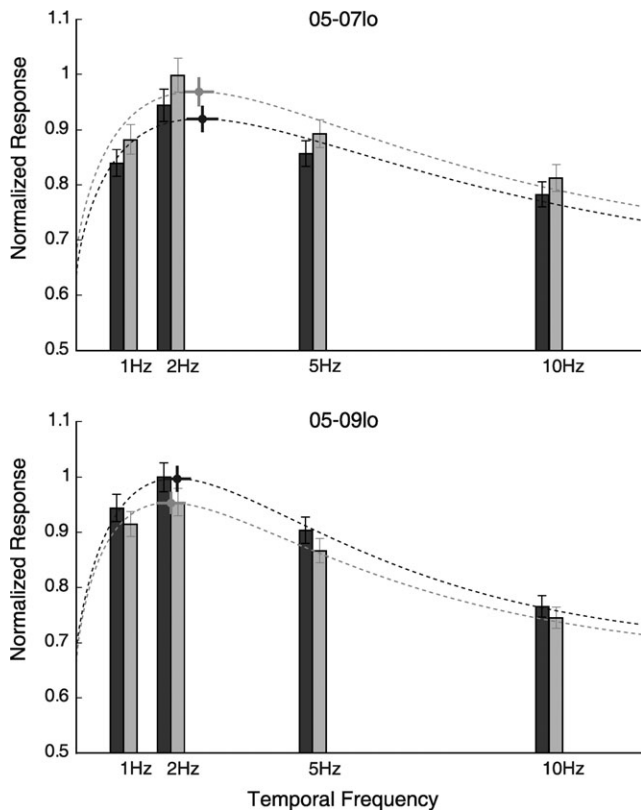


Figure 14. Response strength at different temporal frequencies in blob and interblob subdomains. Two representative examples are shown, with case numbers, above the graphs. The strength of the responses was normalized to the maximum average response for that case. Dotted lines indicate Weibull function fit to the data. A disk with horizontal and vertical bars indicates maximum estimated response at the preferred temporal frequency, with horizontal bar indicating 1 SD in preferred temporal frequency and vertical bar 1 SD in maximum estimated response. Black-CO blob compartment. Gray-CO interblob compartment.

relative stability of attribute maps when different combinations of stimulus properties are examined.

Mapping of Visual Features in Bush Baby

Bush babies are nocturnal primates that lack color vision. They have only a single cone type (Wikler and Rakic 1990; Jacobs et al. 1996; Kawamura and Kubotera 2004) that exists at highest density in the *area centralis* or fovea (Wikler and Rakic 1990). Rods, which are also present in the *area centralis*, predominate in the rest of the retina. Like many nocturnal carnivores including cats and ferrets, bush babies have a well-developed tapetum, and their optimal spatial frequency sensitivity is lower than in macaque monkeys (DeBruyn et al. 1993). The temporal frequency band pass of the bush baby visual system is also low, with a critical flicker-fusion (CFF) frequency of 10–30 Hz (Ordy and Samorajski 1968). This CFF value fits well with single-unit and visual evoked potential data showing that, as demonstrated here, the peak-preferred temporal frequency in V1 is roughly 2 Hz, with a maximum cutoff temporal frequency of 20 Hz (Bonds et al. 1987; DeBruyn et al. 1993). Interestingly, we found that this high temporal frequency cutoff measured with optical imaging could vary from animal to animal, suggesting that some individual bush babies may have more cells representing the higher temporal frequencies than others. It would be interesting to know

whether such variation correlated with individual differences in each animal's capacity to resolve gratings drifted at higher temporal frequencies.

Temporal frequency preference in bush baby is mapped uniformly, at least in the area of V1 representing the central 10–15° of visual space. As mentioned earlier, this is clearly not the case for other feature maps examined in this primate. Spatial frequency, orientation preference, and ocular dominance, mapped using optical imaging, appear to be organized in separate domains in bush baby V1 (Bonds et al. 1987; Xu et al. 2003, 2005, 2007). The only other stimulus feature examined that was not organized into domains in V1 was direction selectivity, even though directional domains were found in the middle temporal visual area in bush babies (Xu, Collins, et al. 2004). It is not clear why some feature maps in this primate show clustering and others do not, especially considering that there appears to be no precise relationships between V1 feature maps that do cluster (see Xu et al. 2005) and given that all features must ultimately be constrained by the necessity of providing adequate coverage across a continuous visual field map (see also below and Horton and Adams 2005).

Functional Maps in Other Species

To date, no other study that used optical imaging was specifically designed to map temporal frequency preference in V1 using drifting grating. Evidence exists that in cats high temporal frequency selectivity measured with stimuli at low spatial frequency is represented separately from low temporal frequency selectivity measured with stimuli at high spatial frequency (Shoham et al. 1997), but other studies using optical imaging have not supported this claim (Everson et al. 1998; Issa et al. 2000; Baker and Issa 2005). Studies using single-unit recording add another dimension, but do not resolve the issue of how these stimulus features are mapped. For example, DeAngelis et al. (1993) found that despite a distribution of preferred spatial and temporal frequency selectivities for individual cells, in young cats (ca. 8 weeks) there is no correlation between preferred spatial and temporal frequencies. As reported earlier by Baker (1990), DeAngelis et al. (1993) also found a negative correlation between spatial and temporal tuning in the adult cat. Neither study, however, examined the issue of whether there was any spatial clustering of stimulus properties in V1 in cats.

Complicating the question of how attributes are represented in V1 of other species is the fact that there appears to be no commonality between the variations seen or an obvious functional reason for them. Because Horton and Adams (2005) recently covered this subject in depth, we will mention only a few relevant points here.

Every mammalian species that has been studied shows a relatively organized map of visual field location in V1 (Chklovskii and Koulakov 2004). There is general agreement that stimulus features that are important for the representation of objects useful for perception must somehow be represented in an iterated fashion across this continuous visual field map in order to avoid holes or gaps in the map (Swindale et al. 2000). The problem is that species appear to have solved the “coverage” problem in different ways even for the same stimulus attribute. Orientation tuning appears to be represented uniformly in all rodents and lagomorphs (e.g., rabbits), even those with well-developed relatively large V1 areas like squirrels (Van Hooser et al. 2005, 2006). Orientation is

represented in a clustered fashion (i.e., pinwheels) in primates and in both diurnal close relatives of primates, tree shrews, and nocturnal distant relatives of primates, cats, and ferrets (Bonhoeffer and Grinvald 1991; Blasdel 1992; Rao et al. 1997; Bosking et al. 2002). Similarly, some species segregate ocular input to V1 into layers (e.g., tree shrews), some segregate eye input into columns (e.g., bush babies), and some show little evidence of either type of segregation (e.g., owl monkeys) (Kaas et al. 1976; Humphrey et al. 1977; Casagrande and Kaas 1994; Xu et al. 2005; but see Rowe et al. 1978).

This conundrum is accentuated by our finding, reported here, that some features, such as temporal frequency selectivity, in bush baby can be mapped uniformly in V1 whereas other features are clustered into domains. It may be that different species have come to different evolutionary solutions to the same problem, but even this explanation does not help to understand the functional significance of the enormous variation seen in some features such as the presence or absence of ocular dominance columns in the same species such as the squirrel monkey (Adams and Horton 2003).

Are Feature Maps Stable?

Still, such enormous variability in how different species map various visual features brings us back to the issues of how many feature maps there really are and how these features are related. As such, one important point which should be considered is the extent to which properties such as selectivity for temporal frequency, spatial frequency, or orientation are hardwired in V1 or represent emergent properties that depend on the stimulus combination presented. In the current study, we examined whether there was an interaction between selectivity for orientation and temporal frequency using high-contrast drifting gratings presented at either 1 fundamental spatial frequency plus its higher spatial frequency harmonics (square-wave gratings) or a single spatial frequency (sine-wave gratings). In either case the result was the same; no evidence was found for different domains devoted to different temporal frequencies.

In another study that examined this issue in ferrets using single-unit recording and sinusoidal grating stimuli, orientation tuning also was found to be invariant to changes in temporal frequency (Moore et al. 2005). In the same study, however, the property of direction selectivity was found to be reduced and sometimes even reversed at nonpreferred temporal frequencies (Moore et al. 2005), which suggests that these features are not hardwired but depend on stimulus conditions. In fact, Basole et al. (2003) used optical imaging in ferret V1 and showed that the same neural population can be activated by multiple combinations of oriented line segment texture patterns and dots depending on the axis of motion of these patterns and their speed. They proposed that, rather than reflecting the intersection of multiple hard wired maps, their results were better explained by considering V1 as a "single map of spatiotemporal energy." These conclusions also were supported by a subsequent modeling study (Mante and Carandini 2005).

Because we did not use more complex stimuli of the sort they describe, we can not address this issue for primates. Regardless, such dynamic maps still do not address the issue raised above concerning species differences seen in maps using the same grating stimuli. Future research will certainly require the use of richer stimulus sets more reminiscent of natural scenes for us to fully understand why stimulus attributes appear to be mapped in V1 in different ways when the same

stimulus is used and how maps relate to each other under normal viewing conditions.

Funding

NIH/NEI EY01778 (V.A.C.); NIH RR13947 (V.A.C.); NIH GM07347 (I.K.); NSF NS044691 (D.W.R.); NIH/NEI EY09223 (R.M.S.); NIH/NEI EY014657 (R.M.S.); Whitehall Foundation 2003-08-12 (R.M.S.).

Supplementary Material

Supplementary Figures 1-8 can be found at: <http://www.cercor.oxfordjournals.org/>

Notes

We would especially like to thank Dr Gopathy Purushothaman for help and suggestions for implementing some of the analysis methods we used. Additionally, we would like to thank Dr Xiangmin Xu, Maria Couppis, Dr Gyula Sary, Ronald Hamrick, and Albert Powers for help with optical imaging experiments. We are grateful to Mary Feurtado for help with animal preparation. We also appreciate Valdimir Enlow's help with proofreading the manuscript. We would especially like to thank Julia Mavity-Hudson for helping with many other aspects of these experiments. Finally, we would like to thank Drs John Gore, Anna Roe, Jon Kaas, Xiangmin Xu, A. B. Bonds, and Gopathy Purushothaman for helpful comments on earlier versions of the manuscript. *Conflict of Interest:* None declared.

Address correspondence to Vivien A. Casagrande, PhD, Department of Cell and Developmental Biology, Vanderbilt Medical School, Vanderbilt University, U3218 Learned Lab, 465 21st Avenue South, Nashville, TN 37232-8240, USA. Email: vivien.casagrande@vanderbilt.edu.

References

- Adams DL, Horton JC. 2003. Capricious expression of cortical columns in the primate brain. *Nat Neurosci.* 6:113-114.
- Baker CL, Jr. 1990. Spatial- and temporal-frequency selectivity as a basis for velocity preference in cat striate cortex neurons. *Vis Neurosci.* 4:101-113.
- Baker TI, Issa NP. 2005. Cortical maps of separable tuning properties predict population responses to complex visual stimuli. *J Neurophysiol.* 94:775-787.
- Basole A, White LE, Fitzpatrick D. 2003. Mapping multiple features in the population response of visual cortex. *Nature.* 423:986-990.
- Berardi N, Bisti S, Cattaneo A, Fiorentini A, Maffei L. 1982. Correlation between the preferred orientation and spatial frequency of neurons in visual areas 17 and 18 of the cat. *J Physiol.* 323:603-618.
- Blasdel GG. 1992. Orientation selectivity, preference, and continuity in monkey striate cortex. *J Neurosci.* 12:3139-3161.
- Bonds AB, Casagrande VA, Norton TT, DeBruyn EJ. 1987. Visual resolution and sensitivity in a nocturnal primate (galago) measured with visual evoked potentials. *Vision Res.* 27:845-857.
- Bonhoeffer T, Grinvald A. 1991. Iso-orientation domains in cat visual cortex are arranged in pinwheel-like patterns. *Nature.* 353:429-431.
- Bonhoeffer T, Grinvald A. 1993. The layout of iso-orientation domains in area 18 of cat visual cortex: optical imaging reveals a pinwheel-like organization. *J Neurosci.* 13:4157-4180.
- Bonhoeffer T, Kim DS, Maloney D, Shoham D, Grinvald A. 1995. Optical imaging of the layout of functional domains in area 17 and across the area 17/18 border in cat visual cortex. *Eur J Neurosci.* 7:1973-1988.
- Bosking WH, Crowley JC, Fitzpatrick D. 2002. Spatial coding of position and orientation in primary visual cortex. *Nat Neurosci.* 5:874-882.
- Bosking WH, Zhang Y, Schofield B, Fitzpatrick D. 1997. Orientation selectivity and the arrangement of horizontal connections in tree shrew striate cortex. *J Neurosci.* 17:2112-2127.

- Boyd JD, Casagrande VA. 1999. Relationships between cytochrome oxidase (CO) blobs in primate primary visual cortex (V1) and the distribution of neurons projecting to the middle temporal area (MT). *J Comp Neurol.* 409:573-591.
- Boyd JD, Matsubara JA. 1996. Laminar and columnar patterns of geniculocortical projections in the cat: relationship to cytochrome oxidase. *J Comp Neurol.* 365:659-682.
- Casagrande VA, Kaas JH. 1994. The afferent, intrinsic, and efferent connections of primary visual cortex in primates. In: Peters A, Rockland KS, editors. *Cerebral cortex*. New York: Plenum Press. p. 201-259.
- Chklovskii DB, Koulakov AA. 2004. Maps in the brain: what can we learn from them? *Annu Rev Neurosci.* 27:369-392.
- DeAngelis GC, Ghose GM, Ohzawa I, Freeman RD. 1999. Functional micro-organization of primary visual cortex: receptive field analysis of nearby neurons. *J Neurosci.* 19:4046-4064.
- DeAngelis GC, Ohzawa I, Freeman RD. 1993. Spatiotemporal organization of simple-cell receptive fields in the cat's striate cortex. I. General characteristics and postnatal development. *J Neurophysiol.* 69:1091-1117.
- DeBruyn EJ, Casagrande VA, Beck PD, Bonds AB. 1993. Visual resolution and sensitivity of single cells in the primary visual cortex (V1) of a nocturnal primate (bush baby): correlations with cortical layers and cytochrome oxidase patterns. *J Neurophysiol.* 69:3-18.
- Duda RO, Hart PE, Stork DG. 2001. *Pattern classification*. New York: Wiley and Sons, Inc.
- Everson RM, Prashanth AK, Gabbay M, Knight BW, Sirovich L, Kaplan E. 1998. Representation of spatial frequency and orientation in the visual cortex. *Proc Natl Acad Sci USA.* 95:8334-8338.
- Horton JC, Adams DL. 2005. The cortical column: a structure without a function. *Philos Trans R Soc Lond B Biol Sci.* 360:837-862.
- Hubel DH, Wiesel TN. 1962. Receptive fields, binocular interaction and functional architecture in the cat's visual cortex. *J Physiol.* 160:106-154.
- Hubel DH, Wiesel TN. 1968. Receptive fields and functional architecture of monkey striate cortex. *J Physiol.* 195:215-243.
- Hubel DH, Wiesel TN. 1974a. Sequence regularity and geometry of orientation columns in the monkey striate cortex. *J Comp Neurol.* 158:267-293.
- Hubel DH, Wiesel TN. 1974b. Uniformity of monkey striate cortex: a parallel relationship between field size, scatter, and magnification factor. *J Comp Neurol.* 158:295-305.
- Hubener M, Shoham D, Grinvald A, Bonhoeffer T. 1997. Spatial relationships among three columnar systems in cat area 17. *J Neurosci.* 17:9270-9284.
- Humphrey AL, Albano JE, Norton TT. 1977. Organization of ocular dominance in tree shrew striate cortex. *Brain Res.* 134:225-236.
- Issa NP, Trepel C, Stryker MP. 2000. Spatial frequency maps in cat visual cortex. *J Neurosci.* 20:8504-8514.
- Jacobs GH, Neitz M, Neitz J. 1996. Mutations in S-cone pigment genes and the absence of colour vision in two species of nocturnal primate. *Proc Biol Sci.* 263:705-710.
- Kaas JH, Lin CS, Casagrande VA. 1976. The relay of ipsilateral and contralateral retinal input from the lateral geniculate nucleus to striate cortex in the owl monkey: a transneuronal transport study. *Brain Res.* 106:371-378.
- Kavamura S, Kubotera N. 2004. Ancestral loss of short wave-sensitive cone visual pigment in lorisiform prosimians, contrasting with its strict conservation in other prosimians. *J Mol Evol.* 58:314-321.
- LeVay S, Nelson SB. 1991. Columnar organization of the visual cortex. In: Leventhal AG, editor. *The neural basis of visual function*. Boston (MA): CRC Press. p. 266-315.
- Mante V, Carandini M. 2005. Mapping of stimulus energy in primary visual cortex. *J Neurophysiol.* 94:788-798.
- Moore BD, Alitto HJ, Usrey WM. 2005. Orientation tuning, but not direction selectivity, is invariant to temporal frequency in primary visual cortex. *J Neurophysiol.* 94:1336-1345.
- Ordy JM, Samorajski T. 1968. Visual acuity and ERG-CFF in relation to the morphologic organization of the retina among diurnal and nocturnal primates. *Vision Res.* 8:1205-1225.
- Rao SC, Toth LJ, Sur M. 1997. Optically imaged maps of orientation preference in primary visual cortex of cats and ferrets. *J Comp Neurol.* 387:358-370.
- Ratzlaff EH, Grinvald A. 1991. A tandem-lens epifluorescence microscope: hundred-fold brightness advantage for wide-field imaging. *J Neurosci Methods.* 36:127-137.
- Rowe MH, Benevento LA, Rezak M. 1978. Some observations on the patterns of segregated geniculate inputs to the visual cortex in New World primates: an autoradiographic study. *Brain Res.* 159:371-378.
- Sakas DE, Charnvises K, Borges LF, Zervas NT. 1990. Biologically inert synthetic dural substitutes. Appraisal of a medical-grade aliphatic polyurethane and a polysiloxane-carbonate block copolymer. *J Neurosurg.* 73:936-941.
- Shoham D, Hubener M, Schulze S, Grinvald A, Bonhoeffer T. 1997. Spatio-temporal frequency domains and their relation to cytochrome oxidase staining in cat visual cortex. *Nature.* 385:529-533.
- Siegel RM, Raffi M, Phinney RE, Turner JA, Jando G. 2003. Functional architecture of eye position gain fields in visual association cortex of behaving monkey. *J Neurophysiol.* 90:1279-1294.
- Swindale NV. 2004. How different feature spaces may be represented in cortical maps. *Network.* 15:217-242.
- Swindale NV, Shoham D, Grinvald A, Bonhoeffer T, Hubener M. 2000. Visual cortex maps are optimized for uniform coverage. *Nat Neurosci.* 3:822-826.
- Van Hooser SD, Heimel JA, Chung S, Nelson SB. 2006. Lack of patchy horizontal connectivity in primary visual cortex of a mammal without orientation maps. *J Neurosci.* 26:7680-7692.
- Van Hooser SD, Heimel JA, Chung S, Nelson SB, Toth LJ. 2005. Orientation selectivity without orientation maps in visual cortex of a highly visual mammal. *J Neurosci.* 25:19-28.
- Weliky M, Bosking WH, Fitzpatrick D. 1996. A systematic map of direction preference in primary visual cortex. *Nature.* 379:725-728.
- Wikler KC, Rakic P. 1990. Distribution of photoreceptor subtypes in the retina of diurnal and nocturnal primates. *J Neurosci.* 10:3390-3401.
- Xu X, Anderson TJ, Casagrande VA. 2007. How do functional maps in primary visual cortex vary with eccentricity? *J Comp Neurol.* 501:741-755.
- Xu X, Bosking WH, Sary G, Stefansic J, Shima D, Casagrande VA. 2004. Functional organization of visual cortex in the owl monkey. *J Neurosci.* 24:6237-6247.
- Xu X, Bosking WH, White LE, Fitzpatrick D, Casagrande VA. 2005. Functional organization of visual cortex in the prosimian bush baby revealed by optical imaging of intrinsic signals. *J Neurophysiol.* 94:2748-2762.
- Xu X, Boyd JD, Gallucci M, Emeric E, Barahimi B, Stefansic J, Shima D, Melzer P, Allison JD, Bonds AB, et al. 2003. Spatial frequency preference maps of primate visual cortex revealed by optical imaging of intrinsic signals. *J Vis.* 3:107.
- Xu X, Collins CE, Kaskan PM, Khaytin I, Kaas JH, Casagrande VA. 2004. Optical imaging of visually evoked responses in prosimian primates reveals conserved features of the middle temporal visual area. *Proc Natl Acad Sci USA.* 101:2566-2571.